In-situ confocal microscopy study of the dissolution kinetics of calcium aluminate inclusions in $CaO-Al_2O_3-SiO_2$ type steelmaking slags

Guang Wang[1]*, Muhammad Nabeel[1], Wangzhong Mu[2,3], A. B. Phillion[1], Neslihan Dogan[1, 4*]

1 Department of Materials Science and Engineering, McMaster University, L8S4L7, Canada

2 Department of Materials Science and Engineering, KTH Royal Institute of Technology, Brinellvagen 23, 10044, Sweden

3 Engineering Materials, Department of Engineering Science and Mathematics, Luleå University of Technology, Luleå, 97187, Sweden

4 Department of Materials Science and Engineering, Delft University of Technology, 2628CD, The Netherlands

* Contact email: wangg84@mcmaster.ca, n.d.dogan@tudelft.nl

Abstract:

Dissolution kinetics of $CaO{\cdot}2Al_2O_3$ (CA2) particles in a synthetic $CaO-Al_2O_3-SiO_2$ steelmaking slag system has been investigated using high-temperature confocal laser scanning microscope (HT-CLSM). Effects of temperatures (i.e., 1500, 1550, and 1600°C) and slag composition on the dissolution time of CA2 particles are investigated, along with the time dependency of the projection area of the particle during the dissolution process. It is found that the dissolution rate was enhanced by either an increase of temperature or a decrease of slag viscosity. Moreover, a higher ratio of CaO/Al_2O_3 (C/A) leads to an increased dissolution rate of CA2 particle at 1600°C. Thermodynamic calculations suggested that the dissolution product, i.e. melilite formed on the surface of the CA2 particle during dissolution in slag with a C/A ratio at 3.8 at 1550°C. SEM-EDS analysis of as-quenched samples confirmed the dissolution path of CA2 particles in slags with C/A ratio at 1.8 and C/A ratio at 3.8 as well as melilite formed on the surface of CA2 particle. The formation of this layer during the dissolution process was identified as a hindrance, impeding the dissolution of CA2 particle. The current study offers a valuable reference for designing or/and choosing the composition of top slag for clean steel production, especially using calcium treatment during the secondary refining process.

Key words: In-situ observation, dissolution kinetics, confocal laser scanning microscope, calcium aluminate inclusions, steelmaking slags, clean steel

1 Introduction

The presence of non-metallic inclusions (NMIs) in steel degrades the final product's mechanical properties, such as tensile strength and corrosion resistance.[1, 2] Moreover, specific types of NMIs can cause some engineering problems, such as clogging of the submerged entry nozzle (SEN) during continuous casting.[3] As a result, it is crucial to minimize the presence of NMIs in steels.

Different approaches have been developed and applied to control and remove NMIs during secondary steelmaking process. Two common approaches are introduced here. The first one is the modification of NMIs' composition and morphology in liquid steel. A well-known example is the calcium treatment for aluminum killed steel, which modifies the solid alumina inclusions to become liquid or semi-liquid calcium aluminates and changes their shape from irregular to spherical. These modifications significantly reduce the risk of SEN clogging and product defects.[4-6] However, inadequate calcium addition can result in incomplete alteration of alumina inclusions, leading to the creation of undesired solid inclusions like $CaO{\cdot}2Al_2O_3$ (CA2) and $CaO{\cdot}6Al_2O_3$ (CA6). If these compounds form, there is an enhanced risk of blockages within the SEN during continuous casting. The second approach is the removal of NMIs from the liquid steel into the molten slag. The removal of NMIs out of the liquid steel can occur in the ladle, tundish, or continuous caster. Irrespective of the process, removal occurs in three stages: 1) flotation of the inclusion from bulk steel to the steel-slag interface, 2) separation of the inclusion from the steel-slag interface, and 3) dissolution of the inclusion into the steelmaking slag. For the last stage, a rapid dissolution of NMIs is desirable. If the dissolution kinetics of NMIs are insufficient, they may oscillate at the slag interface, elevating the risk of re-entrainment.

Over the past few decades, different approaches have been applied to investigate the dissolution of NMIs in the steelmaking slags, especially temperature is the key parameter to be investigated.[7-9] The most common approach is the so-called rotating finger test, or named rotating cylinder test and rotating dip test. For this method, firstly, an oxide cylinder with a diameter of about 1 cm is inserted into the liquid slag, and secondly, the dissolution kinetics are determined from the reduction in the diameter of the cylinder. While this method has provided much insight into NMI's dissolution, a significant limitation is the substantial difference in size between the immersed oxide cylinder and oxide inclusions that occur during the process. Potentially, the difference raises doubts regarding the applicability of data obtained from centimeter-sized samples to dissolution kinetics at micron-scale dimensions.

High-temperature confocal laser scanning microscope (HT-CLSM) is a robust facility that has been developed in the last two decades and provides an in-situ real-time observation capability for investigating the behavior of micron-size NMIs under conditions relevant to the steelmaking process. Sridhar et al.[10] first reported the dissolution process of alumina inclusion in the molten slag. Since then, several studies have been carried out to study the dissolution of different types of inclusion in molten slags. These studies were primarily directed towards the elucidation of the dissolution mechanisms and kinetics of single-phase NMIs including Al_2O_3 [1, 10-21], MgO [1, 13, 15, 22], CaO [23, 24], and SiO_2 [2, 25, 26], as well as the complex NMIs, $MgAl_2O_4$ [1, 13, 15, 27] and Al_2TiO_5 [28-30] in the steelmaking

slag systems, e.g. $CaO-Al_2O_3-SiO_2$ with or without MgO at high temperature ranging from 1250 to 1630 °C. Besides the above mentioned inclusion types, limited information is available in the open literature regarding the dissolution kinetics of calcium aluminate inclusions, e.g., $CaO{\cdot}2Al_2O_3$ (CA2)[6] in steelmaking slags. Miao et al.[6] conducted pioneering research on the dissolution of CA2 in two $CaO-Al_2O_3-SiO_2$ type slags at different temperatures. Their findings indicated that mass transfer of the dissolving species within the molten slag is the rate-limiting step for CA2 dissolution. Furthermore, they observed that the dissolution rate of CA2 was enhanced by higher temperatures and lower SiO_2 content in slag. However, the study employed two types of slags with different C/A (CaO/Al_2O_3) ratios and SiO_2 contents to study the effect of SiO_2 content on the dissolution rate of CA2 particles. This introduces uncertainty regarding the role of the C/A ratio in accelerating CA2 dissolution. Moreover, the impact of one of the most critical factors, the C/A ratio of the refining slag, affecting the total oxygen in molten steel[31], was not explored in relation to the dissolution kinetics of the CA2 particles. Systematic study of the important process parameters is required for a better understanding of the dissolution kinetics and mechanisms of these complex inclusions for achieving clean steel production during the secondary steelmaking process.

This study fills the above-mentioned knowledge gap by combining in-situ observation of CA2 particle dissolution via HT-CLSM, thermodynamic calculations, and electron microscopy. The effect of temperature and slag properties (C/A) ratio and slag viscosity) was quantified. Moreover, the dissolution path of CA2 in two slags at 1550ºC was determined.

2 Methodology

2.1 Materials

Steelmaking type slags were synthesized in the laboratory using high purity (>99.5%) laboratory-grade powders of $CaCO_3$, CaO, SiO_2 and Al_2O_3 obtained from Alfa Aesar, USA. The CaO powder was roasted at 1100°C for 12 hours under air before use to eliminate moisture and decompose any residual $CaCO_3$ present in the powder.

2.1.1 CA2 particle preparation

For the preparation of CA2 particles, a total of 100 g of $CaCO_3$ and Al_2O_3 powder in stochiometric proportions, were prepared. The mixture underwent a mixing process to get the well mixed powder. The details of the mixing process can be found elsewhere.[6] The powder was lightly moistened with approximately 5% distilled water. Approximately 20 g of the dried and moistened powder was compacted into a pellet with a diameter of 2.5 cm and a height of 2 cm. A pressure of 20 MPa was applied for 30 seconds to ensure proper pellet formation. These pellets were then transferred into an alumina crucible and subjected to sintering in a vertical tube furnace. The sintering process involved heating the pellets at a rate of 10°C/min until reaching 1600°C followed by an isothermal hold for 24 h. Subsequently, the pellets were gradually furnace cooled at 10°C/min to room temperature. Throughout the entire

sintering process, argon gas was injected to maintain an inert atmosphere. The sintered pellets were characterized by performing room-temperature powder X-ray Diffraction (XRD) measurements using a PANalytical X'Pert diffraction instrument, which uses a copper source with a wavelength of 1.540 56 Å. A Rietveld refinement of the XRD pattern was performed using the FULLPROF suite. As can be seen in **Fig. 1**, the acquired XRD patterns matched those of the standard reference CA2[32]. Notably, no additional phases were detected, confirming the successful preparation of high-purity CA2.

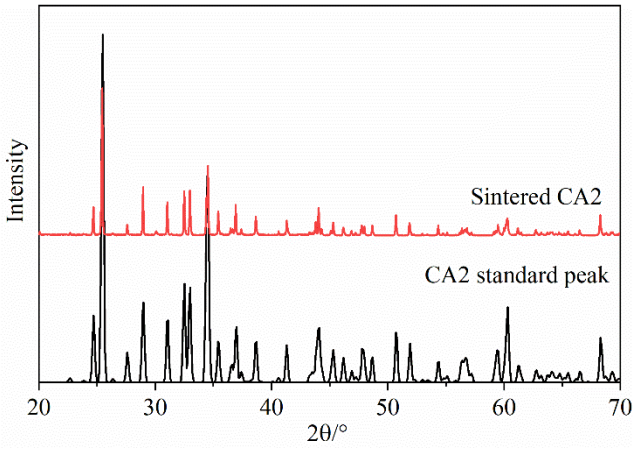

Fig. 1. XRD patterns of CA2 prepared by sintering at 1600°C for 24 h

2.1.2 Slag preparation

Several key factors were considered when designing the slag composition for dissolution experiments using HT-CLSM. First, the slag had to be transparent (or semi-transparent) to enable clear observation of particle dissolution. Second, the liquidus temperature of the slag needed to be lower than that of the inclusions to ensure that the slag was completely liquid and had a homogeneous composition. Finally, slags were designed to provide different C/A ratios and different SiO_2 content. CaO and Al_2O_3 were included to enhance the wettability of the slag with inclusions, while SiO_2 supported the transparency of the slag. Transition-metal oxides such as FeO and CrOx were avoided as they increase the opacity of the slag.

The preparation of slag samples involved mixing powder of CaO, SiO_2, and Al_2O_3 in stochiometric amounts and heating them to the target temperature, i.e., 50°C higher than the theoretical liquidus temperature of the slag. This mixture was fully melted in a platinum crucible placed in a box furnace and then held isothermally for 4 h to ensure homogenization. Post-preparation, the composition of slag was confirmed by inductively coupled plasma optical emission spectroscopy (ICP-OES).

Five different slags were prepared, with the composition shown in **Table 1**. Slag C/A_1, C/A_2, and C/A_4 had a similar SiO_2 content but different C/A ratios to study the effect of C/A ratio on CA2 dissolution kinetics; Slag S50, S40, and S10 had a similar C/A ratio and but different SiO_2 content; these were fabricated to investigate the effect of

slag viscosity on CA2 dissolution kinetics. The influence of temperature on the dissolution of CA2 particles was conducted in slag C/A_1. Please note that slag C/A_2 and S40 are identical. The different nomenclature is used in order to facilitate the discussion of the experimental results.

Table 1 the slag composition and experimental temperatures

Slags	wt.%			C/A	T (°C)
	CaO	Al_2O_3	SiO_2		
C/A_1	29	32	39	0.9	1500, 1550, 1600
C/A_2	38	21	41	1.8	1550, 1600
C/A_4	49	13	38	3.8	1550, 1600
S50	33	18	49	1.8	1550
S40	38	21	41	1.8	1550
S10	52	38	10	1.5	1550

2.2 In-situ observation experiments

An HT-CLSM (VL2000DX-SVF17SP, Yonekura) was employed to perform the dissolution experiments on the CA2 particles while making continuous in-situ observations. The technical details of the HT-CLSM facility and operation procedure can be found elsewhere[33]. The experiment was conducted as follows. Firstly, approximately 0.15 g of slag was pre-melted in a Pt crucible of 5 mm in diameter and 6 mm in height within the high temperature furnace via fast heating and cooling. Secondly, a CA2 particle was placed on the top of the pre-melted slag. Third, the CA2-slag assembly was heated to the test temperature following a specified heating profile. Finally, the dissolution process was recorded via HT-CLSM at a frame rate of 10 Hz. To avoid changing the composition of the slag, the mass of the CA2 particle was kept very small, and less than 0.1% of the pre-melted slag.

Fig. 2 illustrates the entire sample assembly. As can be seen, the Pt crucible, slag, and the CA2 particle were positioned within an alumina crucible, and on top of a sample holder. A B-type thermocouple, sheathed in an alumina tube, was affixed to the base of the sample holder to measure temperature. This setup resulted in a temperature gradient between the slag surface and the bottom of the alumina crucible; temperature calibration was performed by using a pure iron disc 5 mm in diameter and 2 mm in height. This revealed a temperature difference of around +17°C between the surface of the iron disc and the thermocouple. It should be noted that the molten slag wetted the Pt crucible and showed a concave surface; however, this does not affect the observation of the dissolution process.

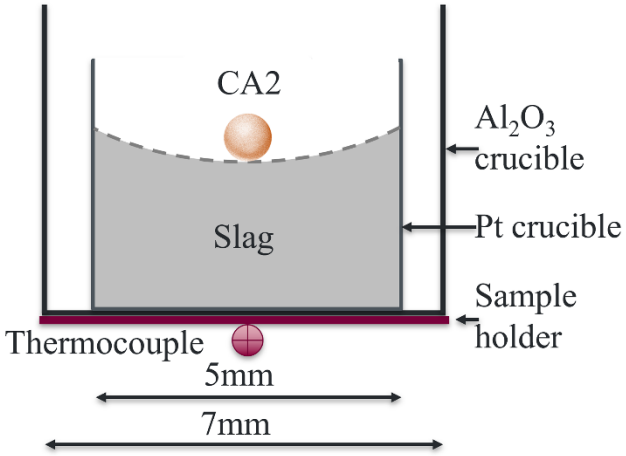

Fig. 2. The sample holder assembly used in the high temperature furnace

Each test followed the same thermal profile, as shown in **Fig. 3**. A rapid heating rate of 1000°C/min was used to elevate the sample temperature to a value of 50°C lower than each testing temperature. Subsequently, a lower heating rate of 50°C/min was used to heat the sample to the testing temperature. This approach served to mitigate the premature dissolution of CA2 particle without overheating past the desired temperature. To ensure experimental repeatability, the dissolution experiments conducted in slag C/A_1 at 1550°C were repeated 4 times. Note that the onset time of CA2 dissolution, t_0, was defined as the moment the particle was fully immersed in the molten slag after reaching the testing temperature. Furthermore, the dissolution path of the CA2 particles in slag C/A_2 and C/A_4 at 1550°C was interrupted after 90 s and 70 s dissolution by quenching the system using helium with a cooling rate at 2000°C/min, respectively. After the experiments were completed, SEM-EDS microanalysis was performed on the two quenched samples using a JEOL6610LV. Thermodynamic calculations were carried out using FactSage 8.0[34]. These calculations included generation of ternary phase diagram, and the determination of slag viscosity using the FToxid databases.

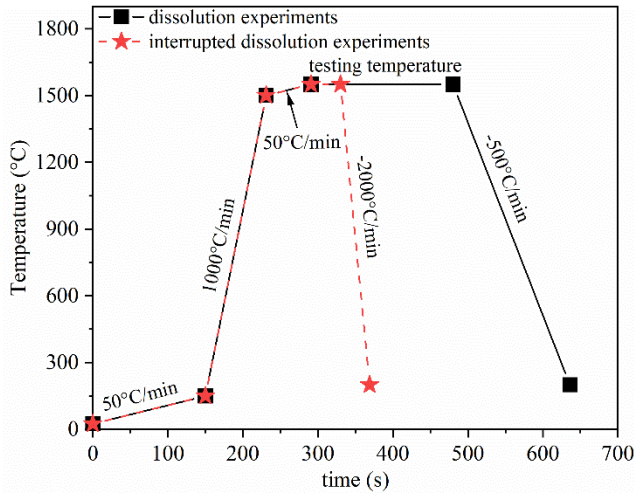

Fig. 3. The thermal cycle for dissolution and interrupted experiments employed in this study

3 Results and discussion

3.1 In-situ observations experiments

In-situ images taken from the CCD camera are used for the evolution of the cross-section area of a CA2 particle. It is critical that the chosen images focus on the same surface of the CA2 particle throughout any one dissolution experiment. The area measurements were conducted using the commercial software ImageJ [35]. To minimize manual error, each image's measurement was repeated three times, and the average value was calculated. Note that the measurements represent the 2D projection area from the view observable via HT-CLSM.

Fig. 4 provides a sequence of images showing the dissolution process of CA2 in (a) the C/A_1 at 1500°C, 1550°C, and 1600°C, b) in slags with different viscosities at 1550°C, and c) in slags with different C/A ratios at 1600°C. Each image within the figure depicts the CA2 particle positioned centrally, with the red line denoting the CA2 particle-slag boundary. The initial area of the CA2 particle at t_0 is denoted as A_0. Across all three series of experiments, a continuous reduction in area with time is observed, with no discernible product layer evident on the surface of the CA2 particle. The equivalent radius (r) of CA2 was calculated according to the area assuming CA2 is spherical. As shown in **Fig. 4a)**, the dissolution time at high temperatures is much shorter than at low temperatures. Further, as shown in **Fig. 4b)**, a decrease in slag viscosity enhances the dissolution time reduction. Note that semi-transparent S10, owing to its low SiO_2 content, results in a less distinct boundary line between CA2 particles compared to other slags. Finally, as shown in **Fig. 4c)** a higher C/A ratio slag qualitatively correlates with a decreased dissolution time. It is interesting to observe that the CA2 particle in slag C/A_2 progressively became transparent during dissolution. This phenomenon could potentially be attributed to the faster transport of Ca^{2+} cations compared to AlO_x^{y-} anions in the molten slag[36]. A similar phenomenon was also observed by Liu et al.[22] for the dissolution of a MgO particle in the ternary CaO-Al_2O_3-SiO_2 slag at 1600°C.

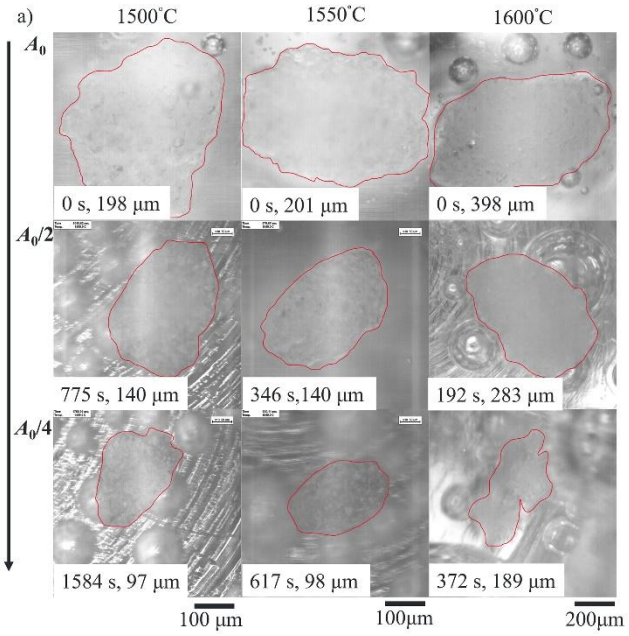
a)
1500°C
1550°C
1600°C
A_0
$A_0/2$
$A_0/4$
0 s, 198 μm
0 s, 201 μm
0 s, 398 μm
775 s, 140 μm
346 s,140 μm
192 s, 283 μm
1584 s, 97 μm
617 s, 98 μm
372 s, 189 μm
100 μm
100μm
200μm

185

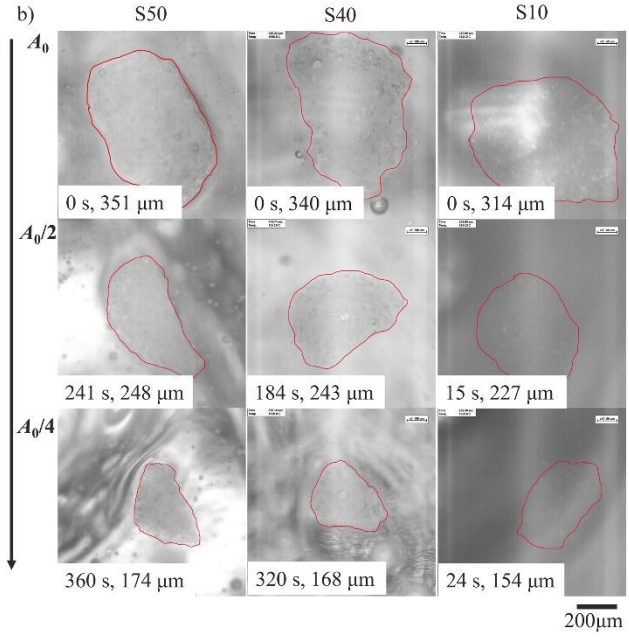
b)
S50
S40
S10
A_0
$A_0/2$
$A_0/4$
0 s, 351 μm
0 s, 340 μm
0 s, 314 μm
241 s, 248 μm
184 s, 243 μm
15 s, 227 μm
360 s, 174 μm
320 s, 168 μm
24 s, 154 μm
200μm

186

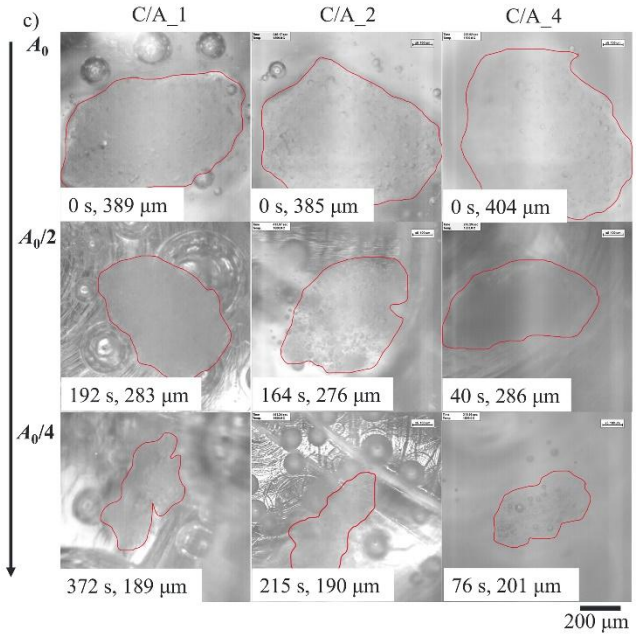

Fig. 4. A sequence of images showing the dissolution process of CA2, a) in slag C/A_1 at 1500°C, 1550°C and 1600°C, b) in slag with different viscosities at 1550°C, and c) in slag with different C/A ratios at 1600°C. s and μm in each sub-image donate dissolution time and the equivalent radius of particle, respectively.

In addition to dissolution, the CA2 particles are observed to rotate, move, and dissociate during experimentation. **Fig. 5** shows one such process, the dissociation of CA2 particle in slag C/A_1 at 1550°C after 846 s of dissolution. At that time, several tiny particles began to detach and move away from the primary particle, as shown in **Fig. 5b**. Then, all particles continued to dissolve in the molten slag, with the small particles disappearing first due to their smaller size. Since the dissolution rate of NMIs is proportional to their contact area with the molten slag,[37, 38] the dissociation of CA2 particles would augment the contact area, leading to a higher dissolution rate. To mitigate the influence of dissociation on the dissolution kinetics, data after CA2 dissociation was excluded from the original dataset in all experiments. This approach enabled isolating the effects of dissociation and ensured a more accurate assessment of dissolution kinetics.

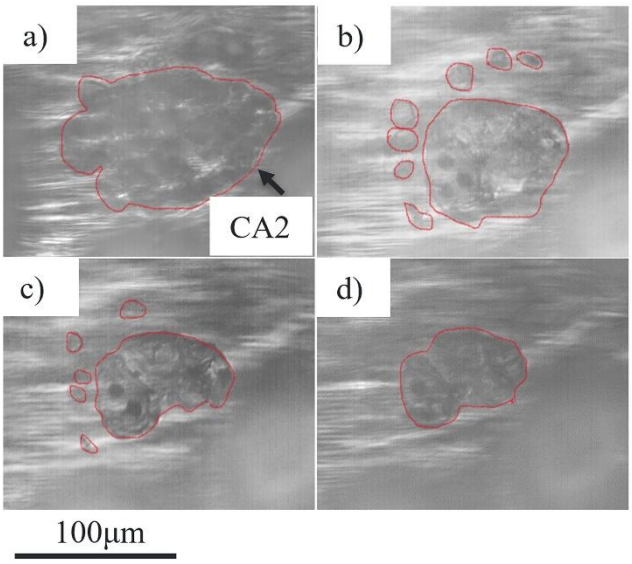

Fig. 5. Dissociation of a particle during dissolution in slag C/A_1 at 1550°C, a) 846 s, b)876 s, c) 897 s and d) 917 s

3.2 Effect of temperature on the dissolution time of CA2 particle

In **Fig. 6**, the normalized area changes with the time of a CA2 particle in the slag C/A_1 at three distinct temperatures are compared. The dissolution time from A_0 to $A_0/4$ significantly decreased from around 1560 s to 617 s, and to 370 s as the temperature increased from 1500°C to 1550°C, and further to 1600°C. The influence of temperature on the dissolution time of particles can be elucidated from both thermodynamic and kinetic perspectives.[14, 16, 17, 20, 23, 24] Thermodynamically, assuming local equilibrium at the particle/slag interface, the driving force for particle dissolution is related to the concentration difference (ΔC) of dissolving species between the particle – slag interface and the bulk of the slag. The former can be evaluated from the phase diagram, given by the saturation limit. The temperature significantly impacts the dissolution rate of particles by changing this driving force; generally, an increase in temperature augments the saturation concentration of particle. In the present study, it is assumed that the driving force for CA2 particle dissolution was the concentration difference between the bulk slag and the saturation content for Al_2O_3 ($\Delta C_{Al_2O_3}$). This assumption is grounded in the fact that the size of the Ca^{2+} cation is smaller than that of the AlO_x^{y-} anion and the diffusion coefficient of Ca^{2+} cation is considerably higher than that of AlO_x^{y-} anion.[36] The $\Delta C_{Al_2O_3}$ increased from 458 kg/m^3 (13 wt.%) to 867 kg/m^3 (25 wt.%) with an increase in temperature from 1500°C to 1600°C. Additionally, the activity of the dissolving component at the particle – slag interface and in the bulk slag can influence the dissolution time as well.[2] In this study, the activity of Al_2O_3 at the particle – slag interface is used as the activity of the reactant Al_2O_3 rather than that in the solid CA2. Using FactSage 8.0 with the FToxid databases[34], the activities of Al_2O_3 in slag C/A_1 at 1500°C, 1550°C, and 1600°C were calculated to be 1.47×10^{-1}, 1.76×10^{-1} ,

2.07×10^{-1} at the particle – slag interface, and 7.11×10^{-2}, 7.43×10^{-2}, and 7.74×10^{-2} in the bulk slag, respectively. These results indicate that the difference in Al_2O_3 activity between the particle-slag interface and bulk slag increases as the temperature rises. The increase in this difference results in improved mobility of the AlO_x^{y-} anion within the molten slag, thereby reducing the overall dissolution time.

From the kinetic perspective, temperature changes will also strongly affect the rate of chemical reaction and/or boundary layer diffusion. For a first-order chemical reaction, the rate of particle dissolution is given by:

$$J = k * C_1 \quad (1)$$

where J is the molar flux of particle per unit area, k is a rate constant, and C_1 is the concentration difference of the dissolving species between solid oxide and bulk slag. For boundary layer diffusion, Fick's first law can be applied to the diffusion across the boundary layer. In this case, the rate of particle dissolution is given by:

$$J = -D * \frac{C_2}{\delta} \quad (2)$$

where D is the diffusion coefficient of dissolving species, and C_2 is the concentration difference of the dissolving specie between the inside and outside of the boundary layer with thickness δ. An Arrhenius relation describes the temperature dependency of both k and D:[14]

$$k = k_0 * e^{-E_{a1}/(RT)} \quad (3)$$

$$D = D_0 * e^{-E_{a2}/(RT)} \quad (4)$$

where k_0 and D_0 are constants, E_{a1} and E_{a2} are activation energies, R is the universal gas constant, and T is the absolute temperature. It is clear from Eqs. (3) and (4) that k and D increase with increasing temperature and therefore so does J, and by extension the dissolution rate. In addition to the change in driving force, viscosity impacts the dissolution rate as well. By increasing the temperature from 1500°C to 1600°C, the slag viscosity was calculated to decrease from 3.12 to 1.32 Pa·s. The elevated $\Delta C_{Al_2O_3}$ and activity difference, and reduced viscosity are conducive to accelerate the transport of AlO_x^{y-} from the CA2 – slag interface to the bulk slag. [2, 6, 20]

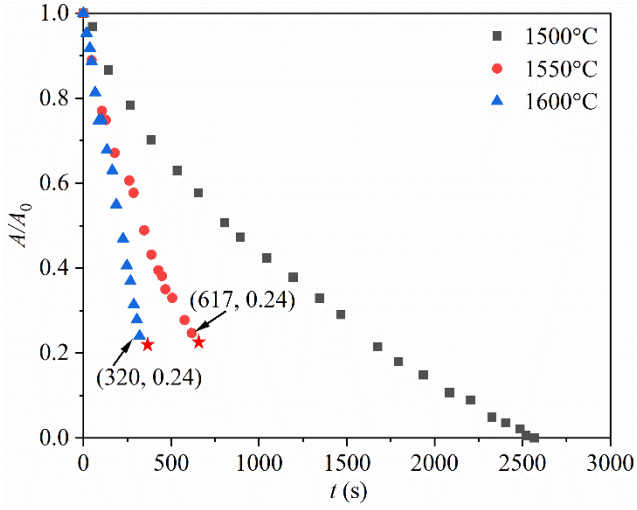

Fig. 6. The evolution in the normalized area of a CA2 particle with time in slag C/A_1 as a function of temperature. Star symbol illustrates the moment when particle dissociation happened, and the data after that point is not collected.

3.3 Effect of slag viscosity on the dissolution time of CA2 particle

As shown in Fig. 7, the total dissolution time of the CA2 particle at 1550˚C exhibited a slight decrease from 800 s to 650 s as the viscosity of the slag decreased from 1.35 Pa·s (S50) to 0.63 Pa·s (S40). A further reduction in the slag viscosity to 0.17 Pa·s (S10) resulted in a substantial drop in the total dissolution time to 37 s. The change in dissolution time could be a result of two phenomena: (1) the concentration difference of the dissolving species between the particle – slag interface and the bulk of the slag since each of these slags has a different composition, or (2) the underlying slag structure which directly controls the viscosity (along with slag composition and temperature).

Examining the first phenomenon, it can be seen that the decrease of $\Delta C_{Al_2O_3}$ in kg/m^3 from S50 (1481 kg/m^3, 32 wt.%) to S40 (887 kg/m^3, 26 wt.%) is much larger than the decrease from S40 to S10 (801 kg/m^3, 22 wt.%). This trend is opposite to what was observed for the total dissolution time, and thus, the decrease in the total dissolution time is not so much affected by the change of $\Delta C_{Al_2O_3}$. Miao et al.[6] also reported that the total dissolution time for CA2 in CaO-Al_2O_3-SiO_2 slag with 5.5% SiO_2 content was shorter than that in a slag with 46.3% SiO_2 content at the same temperature, despite the $\Delta C_{Al_2O_3}$ being lower in the 5.5% SiO_2 slag.

Examining the second phenomenon requires a short review of slag structure. One approach is to analyze slag structure through polymer- and structure- based theories [39], where the slag structure is affected by the content of different oxides present in the slag as they strongly affect the degree of polymerization. SiO_2 is an “acid oxide”, and forms an intricate three-dimensional network of anion complexes, whereas CaO is a “basic oxide”, and disrupts the three-dimensional networks formed from the SiO_2 oxides. Finally, Al_2O_3 is classified as an “amphoteric oxide” which does not have any distinctive nature. The higher content of network formers, SiO_2 in S50 and S40, significantly surpasses that of S10, while the content of network breakers, like CaO, in S50 and S40 is lower than that in S10. As a result, the presence of complex three-dimensional networks in S10 was comparatively reduced, resulting in making it easier for species to transport away from the interface in S10 as compared to in S40 and S50. This reduced resistance facilitates faster dissolution of a CA2 particle in S10. The degree of polymerization can be quantified using the Q parameter, which in the CaO-Al_2O_3-SiO_2 slag system is determined via [36]:

$$Q = 4 - NBO/X_T \quad (5)$$

$$NBO = 2(X_{CaO} - 2X_{Al_2O_3}) \quad (6)$$

$$X_T = X_{SiO_2} + 2X_{Al_2O_3} \quad (7)$$

where NBO is the number of non-bridge oxygen atoms, X_T is the number of tetragonally-coordinated atoms, and X_i is the molar ratio of component i in the slag. A higher Q indicates a greater degree of polymerization of the molten slag and consequently, reduced mobility of dissolving species within the slag. The Q value for S10 is 2.7, contrasting with 3.3 for S50 and 3.2 for S40. This disparity potentially enhances the transport of AlO_x^{y-} anions from the CA2 particle-slag interface to the bulk slag, thereby significantly accelerating the dissolution process in S10 as compared to that in

S40 and S50. Therefore, similar Q values would result in close dissolution profiles of S50 and S40. Moreover, as discussed in [40], Q values between 3 to 4 result in a slag structural unit known as "sheet" whereas slag with Q values between 2 to 3 have a structural unit known as "chain". As a result, the significant decrease in total dissolution time from S40 to S10 slags is primarily affected by the change in slag structure. Finally, it should also be noted that the particle in the S10 experiment was observed to be rotating much faster than the particles in the S40 and S50 experiments. This could also have affected the dissolution time.

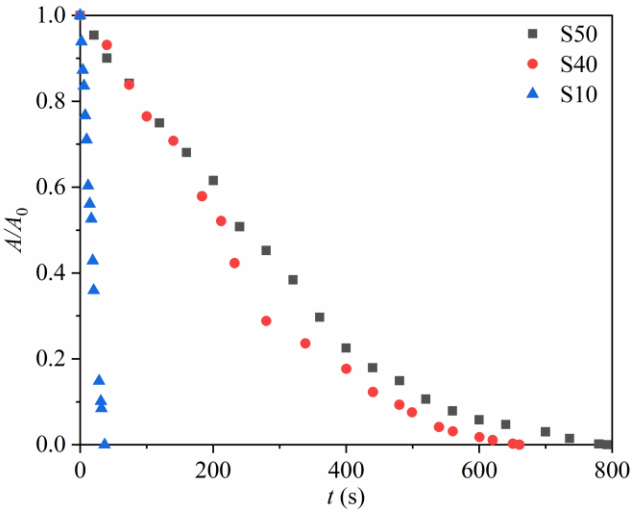

Fig. 7. The evolution in the normalized area of a CA2 particle with time at 1550°C in slags with different SiO_2 contents, having different viscosities

3.4 Effect of C/A ratio on the dissolution time of CA2 particles

The effect of the C/A ratio on the dissolution of CA2 particles was investigated in three slags having C/A ratios of 0.9, 1.8, and 3.8, each possessing similar SiO_2 content (~40%) at 1600°C and 1550°C, respectively. **Fig. 8a)** illustrates the normalized area change of CA2 particles with time at 1600°C. As can be seen, the dissolution time from A_0 to $A_0/4$ of CA2 at 1600°C decreased from around 315 s to 81 s by increasing the C/A ratio from 0.9 to 3.8. This decrease in dissolution time can be attributed to the continuous decrease in slag viscosity from 1.32 Pa·s to 0.17 Pa·s, coupled with an increase in the $\Delta C_{Al_2O_3}$ from 867 kg/m^3 (25 wt.%) to 1271 kg/m^3 (40 wt.%) as the C/A ratio increased from 0.9 to 3.8. Both factors, low viscosity, and high driving force, enhanced the dissolution of the CA2, resulting in a shortened dissolution time. **Fig. 8b)** depicts the normalized area change with time in slags with different C/A ratios at 1550°C. Initially, the dissolution time A_0 to $A_0/4$ of CA2 particle decreased from 617 s to 340 s with an increase in C/A ratio from 0.9 to 1.8. This decrease can be attributed to a reduction in slag viscosity from 2.00 Pa·s to 0.63 Pa·s, coupled with an increase in $\Delta C_{Al_2O_3}$ from 606 kg/m^3 (18 wt.%) to 887 kg/m^3 (49 wt.%). These factors collectively promote the

dissolution of the CA2 particle. However, with a further increase in the C/A ratio to 3.8, the dissolution time unexpectedly increased to 710 s. At this C/A ratio, the viscosity was further decreased to 0.22 Pa·s, and the $\Delta C_{Al_2O_3}$ dropped to 372 kg/m^3 (26 wt.%). This unexpected behavior suggests that factors beyond $\Delta C_{Al_2O_3}$ and slag viscosity may influence the dissolution kinetics of the CA2 particle at higher C/A ratios.

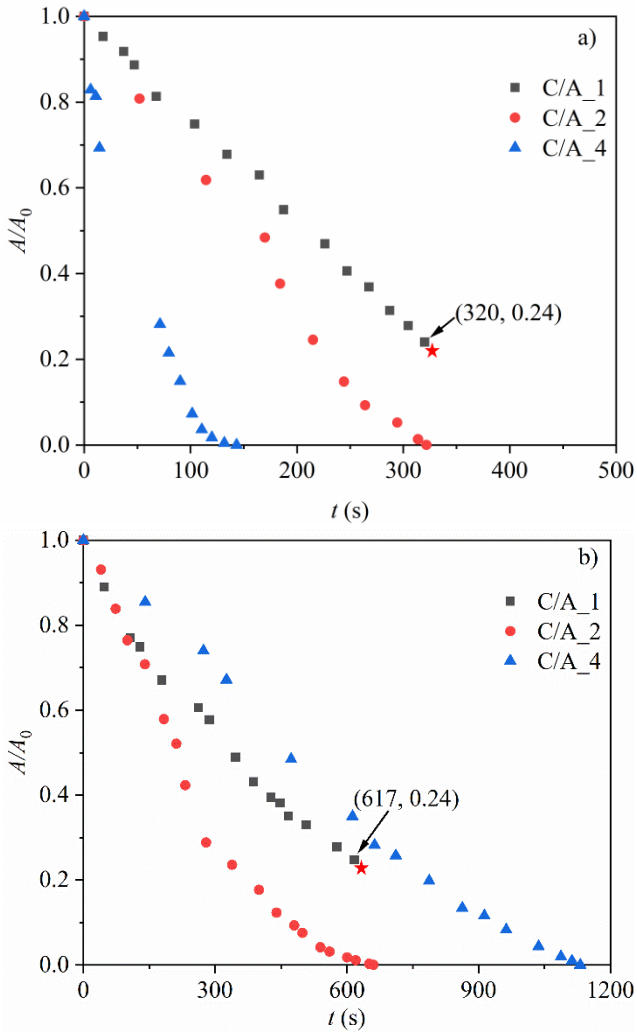

Fig. 8. The evolution of the normalized area of a CA2 particle with time as a function of slag C/A ratio at a)1600°C, b) 1550°C. Star symbol illustrates the moment when particle dissociation happened, and the data after that point is not collected.

To gain increased insight into the effects of the C/A ratio on the dissolution of CA2 at 1550°C, the stable phases potentially present in the CA2 – SiO_2-Al_2O_3-CaO system at this temperature were calculated using FactSage 8.0 with FToxid database[34]. **Fig. 9** shows the relevant ternary diagram, marked with the composition of CA2, and the initial compositions of slags C/A_1, C/A_2, and C/A_4, as well as black solid lines denoting the two-phase tie lines, dashed lines denoting the expected dissolution paths of CA2 in the three slags, and the melilite and CA6 solid phase regions.

Although the dissolution is inherently a non-equilibrium process and the dissolution path does not have to be a straight line, the phase diagrams allow for the prediction of phases that may precipitate adjacent to the CA2 particle.

As can be seen in **Fig.9**, at 1550°C, the composition of all three slags was situated within the fully liquid region. However, the expected dissolution path for slag C/A_1 comes very close to the solid CA6 phase boundary, while the dissolution path for slag C/A_4 crosses through the solid melilite phase boundary. Thus, the formation of intermediate solid products during the dissolution process, especially for C/A_4, is anticipated. Generally, the formation of an intermediate solid phase on the surface of a solid particle can impede the dissolution of particles by decreasing the transport rate of products from and reactants to the particle surface.[23] In extreme cases, solid products may halt the dissolution if they are densely packed on the particle surface and do not dissolve into the bulk slag. It would appear that the formation of a solid layer on the surface of the CA2 particle during its dissolution in slag C/A_4 at 1550°C, which could have contributed to the observed prolonged dissolution time.

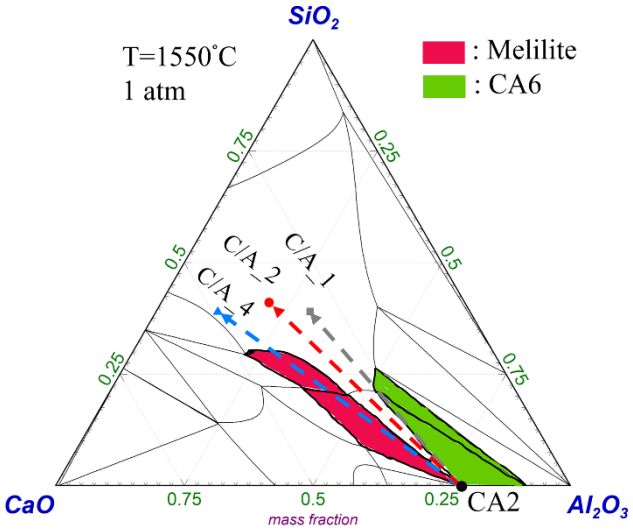

Fig. 9. Prediction of phase stability of the CA2 particle-slag system with FactSage 8.0[34] at 1550°C

3.5 Determination of the dissolution path

To gain deeper insights into the dissolution path of a CA2 particle in slag C/A_2 and slag C/A_4, SEM-EDS line scan analysis was conducted along the CA2 particle/slag interface and combined with FactSage thermodynamic calculations. The results are shown in **Figs. 10-12**. In order to interpret the line scan information with respect to the dissolution path, a mechanism for distinguishing the CA2 particle, slag C/A_2, slag CA_4, and melilite must be identified. As shown in **Table 2**, each of these compounds has a distinct elemental composition. Thus, in the CA2 particle – slag C/A_2 system, regions at the particle/slag interface that lack Si can be classified as CA2, while regions where Ca, Al, and Si stably coexist can be labeled as slag C/A_2. Boundary layers are regions having a decreasing Ca

and Si composition while the Al content steadily increases. Similarly, in the CA2 particle – C/A_4 slag system, the non-Si regions at the particle/slag interface can be designated as CA2, while regions where Ca, Al, and Si coexist, with Al and Si constituting ~20 wt.% and ~10 wt.%, can be identified as melilite. All other regions can be classified as slag C/A_4.

Table 2 The elemental composition (wt.%) of CA2 particle, slag C/A_2, slag CA_4 and melilite at 1550°C

Wt.%	Ca	Al	Si
CA2	15	42	0
C/A_2	27	11	19
C/A_4	34	7	17
Melilite	29	20	10

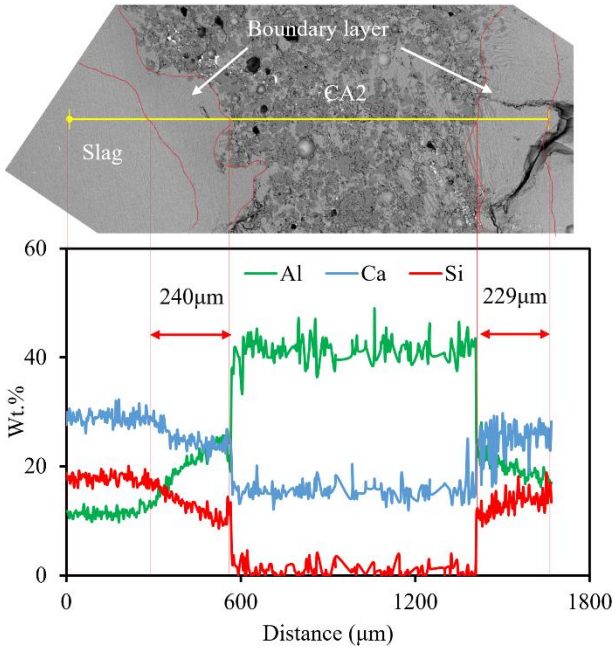

Fig. 10. SEM back scattered electron image and EDS line scan analysis of CA2 particle - CA_2 slag interface after 90 s dissolution at 1550°C

Fig. 10 displays the SEM back scattered electron image, and the elements Ca, Al, and Si distribution obtained from the EDS line scan of the CA2 particle – C/A_2 slag interface after 90 s of dissolution at 1550°C. Following the defined criteria, different regions were identified. The dark-colored middle region in the SEM image represents CA2. An outer layer around the CA2 particle was determined to be the boundary layer, with a thickness of 230 μm to 240 μm. The

C/A_2 slag region followed the boundary layer. Moreover, a visible color difference between the slag and the boundary layer was evident in the SEM image. The presence of a boundary layer confirmed that the assumption of the rate determining step for the dissolution process is the mass transfer of AlO_x^{y-} anion in the slag phase. Note that fluctuations in element concentration, especially within the CA2 particle itself, result from slag penetration into the CA2 particle through its pores.

Fig. 11 shows the SEM back scattered electron image and the elements Ca, Al, Si distribution by EDS line scan of CA2 particle – C/A_4 slag interface after 70 s of dissolution at 1550°C. As can be seen, there is the CA2 particle in the central region, followed by a layer of melilite 105 µm -111 µm in thickness, and then a boundary layer of about 115 µm.

Fig. 12 shows the dissolution paths of CA2 in slag C/A_2 (circle symbol) and slag C/A_4 (triangle symbol) at 1550°C. The data points donated by circle and triangle symbols were taken from the EDS results for both slag systems at different regions along the scanned line. The dashed lines in **Fig. 12** donate the theoretical dissolution paths for CA2 in these two slags. It is evident that the prolonged dissolution of CA2 in slag C/A_4 compared to slag C/A_2 at 1550°C is attributed to the formation of the solid melilite phase on the surface of the CA2 particle. The same reaction product melilite for Al_2O_3 dissolution at 1550°C was also reported by Park et al.[41] in a ternary 53CaO-5Al_2O_3-42SiO_2 (wt.%) slag and by Sandhage et al.[42] in a quaternary 27CaO-21Al_2O_3-42SiO_2-10MgO (wt.%) slag, which retarded the dissolution of Al_2O_3.

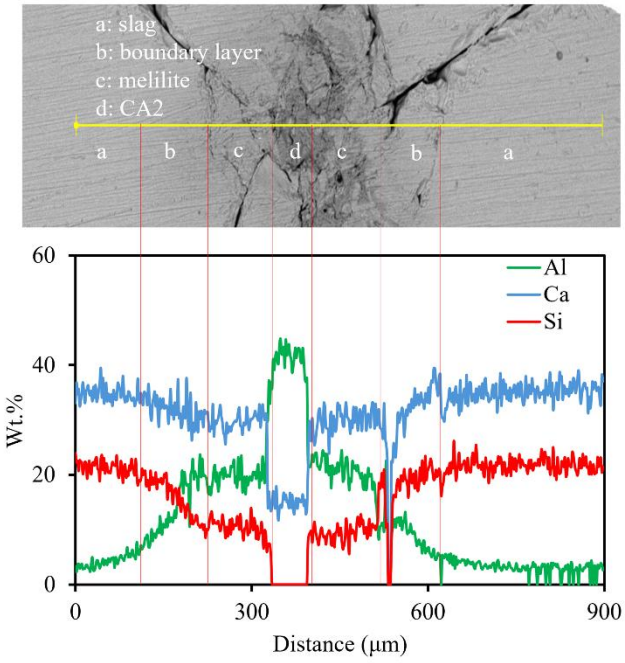

Fig. 11. SEM back scattered electron image and EDS line scan analysis of CA2 particle - CA_4 slag interface after 70 s dissolution

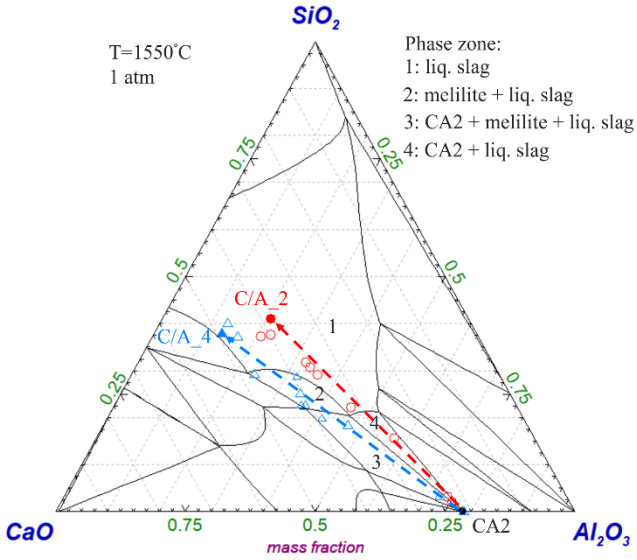

Fig. 12. The dissolution paths of CA2 in slag C/A_2 and slag C/A_4 at 1550°C (circle and triangle indicating EDS line scan results, dash line indication thermodynamic calculation results)

3.6 Comparison with literature data and practical consideration

The dissolution kinetics between Al_2O_3 and CA2 particles from the literature and current study were compared since the assumption is that the driving force for CA2 particle dissolution is the concentration difference between the bulk slag and the saturation content for Al_2O_3 ($\Delta C_{Al_2O_3}$), which is the same as that for Al_2O_3 dissolution. **Fig. 13** illustrates the average area reduction rate, $\Delta A/\tau$, change as a function of the dissolution factor, $(\Delta C_{Al_2O_3})/\mu$. ΔA is area change of CA2 during the dissolution time, τ, before dissociation happens in comparison with the A_0. As can be seen at low $(\Delta C_{Al_2O_3})/\mu$ value (< 1000), the difference of $\Delta A/\tau$ between Al_2O_3 and CA2 particles is small, and it becomes noticeable when $(\Delta C_{Al_2O_3})/\mu$ value is higher than 1000. This difference in the $\Delta A_0/\tau$ may be due to 1) the greater porosity of lab produced CA2 particles compared to commercially available dense Al_2O_3 particles; 2) the faster dissolution of CaO in CA2 particles, which exposes more Al_2O_3 surface to the liquid slag, increasing the contact area between CA2 particle and molten slag. Moreover, the dissolved CaO from CA2 particles can act as a network breaker, enhancing the mobility of molten slag.

In the present dissolution experiments, CA2 particles were only immersed and dissolved into the molten slag under natural convection without any additional forces. In practical applications, the inclusion dissolution typically occurs at the molten steel/top slags interface during the steel refining process, at the steel/tundish slags interface, as well as at the steel/mold fluxes interface during casting, conditions that more closely resemble natural convection. When the

melilite phase forms an out layer around the CA2 particle, the CA2 dissolution rate is slower than in other cases at the same temperature. The authors believe that the experimental conditions in this study are relevant to the industrial conditions and the findings offer a valuable reference for designing or/and choosing the composition of top slag, tundish slag, and mold fluxes. This is particularly for Al-killed steel with Ca-treatment, where the calcium is fed into molten steel in the final minutes during the secondary steelmaking, necessitating rapid inclusion dissolution by the top slag.

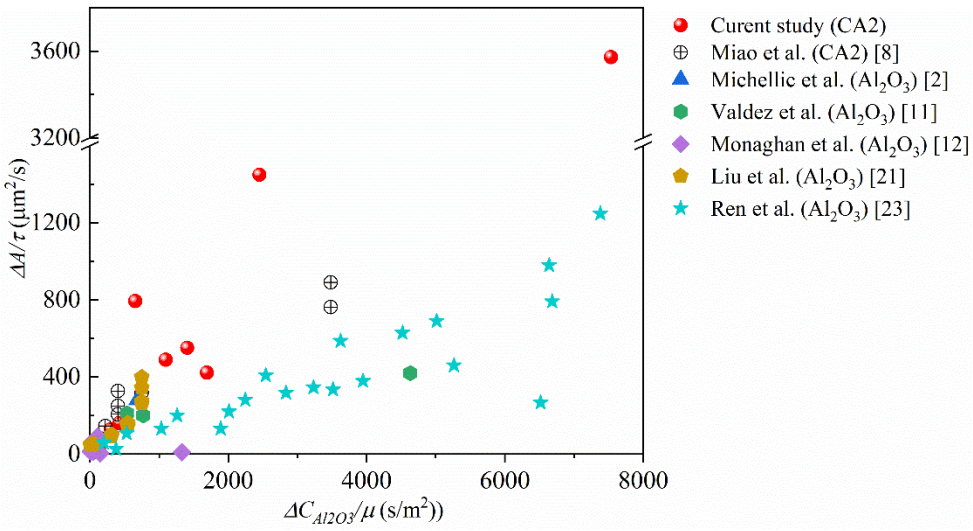

Fig. 13. The average area reduction rate of different types of particles as a function of $(\Delta C_{Al_2O_3})/\mu$

4. Conclusions

Effects of temperature and slag composition on the dissolution kinetics of CA2 particles in the CaO-Al_2O_3-SiO_2 slag system were studied at a temperature range from 1500°C to 1600°C using the HT-CLSM technique. From the in-situ observations, SEM-EDS analysis, and thermodynamic calculations, the following conclusions are made:

1) The increase in temperature enhances the dissolution rate of CA2 across all types of CaO-Al_2O_3-SiO_2 slags. Furthermore, the dissolution rate of CA2 significantly decreases when the SiO_2 content increased from 10% to 40%. However, a further increase to 50% SiO_2 did not significantly influence the dissolution rate.
2) The significant decrease in total dissolution time from the slag with 40%SiO_2 to the slag with 10%SiO_2 is primarily affected by the change in slag structure.
3) At 1600°C, a higher C/A ratio leads to an increased CA2 dissolution rate. However, it was observed that the formation of melilite layer during the dissolution process acts as a hindrance, impeding the dissolution of the CA2 particle at 1550°C.
4) The presence of a boundary layer at the CA2 particle – C/A_2 slag interface is identified as a solid melilite phase which was observed at the surface of the CA2 particle in the CA2 particle – C/A_4 slag system. These

observations are consistent with the thermodynamic predictions, validating the accuracy of the experimental and analytical methodologies employed.

Acknowledgments

The authors would like to thank the Natural Sciences and Engineering Research Council of Canada (NSERC) for funding this research. This research used a high temperature confocal laser scanning microscope-VL2000DX-SVF17SP funded by Canada Foundation for Innovation John Evans Leaders Fund (CFI JELF, Project Number: 32826), a PANalytical X'Pert diffraction instrument located at the Centre for crystal growth, Brockhouse Institute for Materials Research, and a scanning electron microscope-JEOL 6610 located at the Canadian Centre for Electron Microscopy at McMaster University. W. Mu would like to acknowledge Swedish Iron and Steel Research Office (Jernkonteret), STINT and SSF for supporting the time for international collaboration research regarding clean steel.

Statements and Declarations

On behalf of all authors, the corresponding author states that there is no conflict of interest.

Reference

1. K. Prapakorn M. Valdez, A W. Cramb, S. Seetharaman: *Steel Res. Int.* 2001, vol. 72, pp. 291-97.
2. S.K. Michelic S. Feichtinger, Y.B. Kang, C. Bernhard: *J. Am. Ceram. Soc.* 2014, vol. 97, pp. 316-25.
3. S. Waterfall S. Sun, N. Strobl, D. Liao, D. Holdridge: In *8th International Symposium on High-Temperature Metallurgical Processing*, Springer: 2017, pp 347-57.
4. L. Zhang W. Yang, X. Wang, Y. Ren, X. Liu, Q. Shan *ISIJ Int.* 2013, vol. 53, pp. 1401-10.
5. Y. Liu L. Zhang, Y. Zhang, W. Yang, W. Chen: *Metall. Mater. Trans. B* 2018, vol. 49, pp. 1841-59.
6. K. Y. Miao, A. Haas, M. Sharma, W. Z. Mu, and N. Dogan: *Metall. Mater. Trans. B* 2018, vol. 49, pp. 1612-23.
7. P.T. Jones M. Guo, S. Parada, E. Boydens, J.V. Dyck, B. Blanpain, P. Wollants,: *J. Eur. Ceram. Soc.* 2006, vol. 26, pp. 3831-43.
8. A.G.Martinez M.A. Braulio, A.P.Luz, C. Liebske, V.C. Pandolfelli: *Ceram. Int.* 2011, vol. 37, pp. 1935-45.
9. C.E. Cicutti Y. Kashiwaya, A.W. Cramb, K. Ishii, : *ISIJ Inter.* 1998, vol. 38, pp. 348-56.
10. A.W. Cramb S. Sridhar: *Metall. Mater. Trans. B* 2000, vol. 31, pp. 406-10.
11. K Prapakorn M Valdez, AW Cramb, S Sridhar: *Ironmaking Steelmaking* 2002, vol. 29, pp. 47-52.
12. C. Tse K.W. Yi, J.H. Park, M. Valdez, A.W. Cramb, S. Sridhar: *Scand. J. Metall.* 2003, vol. 32, pp. 177-84.
13. J. Gisby A.B. Fox, R.C. Atwood, P. D. Lee, S. Sridhar: *ISIJ Inter.* 2004, vol. 44, pp. 836-45.
14. L. Chen B.J. Monaghan: *J. Non-Cryst. Solids* 2004, vol. 347, pp. 254-61.
15. L. Chen B. J. Monaghan, J. Sorbe: *Ironmaking steelmaking* 2005, vol. 32, pp. 258-64.
16. L. Chen B.J. Monaghan: *Steel Res. Int.* 2005, vol. 76, pp. 348-54.
17. M. Guo J. Liu, P.T. Jones, F. Verhaeghe, B. Blanpain, P. Wollants *J. Am. Ceram. Soc.* 2007, vol. 90, pp. 3818-24.

18. F. Verhaeghe; J. Liu; M. Guo; S. Arnout; B. Blanpain; P. Wollants: *Appl. Phys. Lett.* 2007, vol. 91, p. 124104.
19. J. Goriupp S. Michelic, S. Feichtinger, Y.B. Kang, C. Bernhard, J. Schenk: *Steel Res. Int.* 2016, vol. 87, pp. 57-67.
20. L. Zhang C. Ren, J. Zhang, S. Wu, P. Zhu, Y. Ren: *Metall. Mater. Trans. B* 2021, vol. 52, pp. 3288-301.
21. C. Huang C. Ren, L. Zhang, Y. Ren: *Int. J. Miner., Metall. Mater.* 2023, vol. 30, pp. 345-53.
22. M. Guo J. Liu, P.T. Jones, F. Verhaeghe, B. Blanpain, P. Wollants: *J. Eur. Ceram. Soc.* 2007, vol. 27, pp. 1961-72.
23. ZHI Sun X Guo, J Van Dyck, M Guo, B Blanpain: *Ind. Eng. Chem. Res.* 2014, vol. 53, pp. 6325-33.
24. X. Guo Z. Sun, J. Van Dyck, M. Guo, B. Blanpain: *AIChE J.* 2013, vol. 59, pp. 2907-16.
25. Y. Zhang T. Tian, H. Zhang, K. Zhang, J. Li, H. Wang: *Int. J. Appl. Ceram. Technol.* 2019, vol. 16, pp. 1078-87.
26. P. Zhu Y. Ren, C. Ren, N. Liu, L. Zhang: *Metall.Mater.Trans. B* 2022, vol. 53, pp. 682-92.
27. L. Chen B.J. Monaghan: *Ironmaking steelmaking* 2006, vol. 33, pp. 323-30.
28. W. Mu M. Sharma, N. Dogan: *Jom* 2018, vol. 70, pp. 1220-24.
29. H.A. Dabkowska M. Sharma, N. Dogan *Steel Res. Int.* 2019, vol. 90, p. 1800367.
30. N. Dogan M. Sharma: *Metall. Mater.Trans. B* 2020, vol. 51, pp. 570-80.
31. K.H. Heo B.H. Yoon, J.S. Kim, H.S. Sohn: *Ironmaking steelmaking* 2002, vol. 29, pp. 214-17.
32. D.M. Kheiker V.I. Ponomarev, N.V. Belov: *Sovit Physics Crystallogaphy* 1971, vol. 15, pp. 995-1002.
33. H. Shibata H. Chikama, T. Emi, M. Suzuki *Mater. Trans., JIM* 1996, vol. 37, pp. 620-26.
34. C. W. Bale, E. Bélisle, P. Chartrand, S. A. Decterov, G. Eriksson, A. E. Gheribi, K. Hack, I. H. Jung, Y. B. Kang, J. Melançon, A. D. Pelton, S. Petersen, C. Robelin, J. Sangster, P. Spencer, and M. A. Van Ende: *Calphad* 2016, vol. 55, pp. 1-19.
35. W.S. Rasband C.A. Schneider, K.W. Eliceiri: *Nat. Methods* 2012, vol. 9, pp. 671-75.
36. V.D. Eisenhüttenleute: *Slag Atlas*. Slag Atlas, 3rd ed., V.D. Eisenhuttenleute, ed., Slag Atlas, 2nd ed., Verlag Stahleisen GmbH, Dusseldorf, 1995.
37. W Mu C Xuan: *J. Am. Ceram. Soc.* 2019, vol. 102, pp. 6480-97.
38. X. Wang R. Li, X. Gao, W. Wang, Y. Zhou: *Ceram. Int.* 2024, vol. 50, pp. 8249-59.
39. D.R. Gaskell: *Metall. Treatises* 1981, pp. 59-78.
40. Ken Mills: *Southern African Pyrometallurgy* 2011, vol. 7, pp. 35-42.
41. I.H. Jung J.H. Park, H.G. Lee: *ISIJ int.* 2006, vol. 46, pp. 1626-34.
42. Kenneth H Sandhage and Gregory J Yurek: *J. Am. Ceram. Soc.* 1988, vol. 71, pp. 478-89.